Model-based Evaluation of Connexin Hemichannel Permeability

Tadas Kraujalis, Lukas Kersys, Andrius Krisciunas, Dalia Calneryte, Auguste Cicinskaite, Lina Kraujaliene, Vytas K. Verselis, Mindaugas Snipas

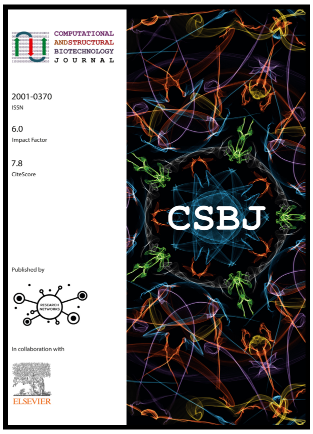

PII: S2001-0370(25)00537-9
DOI: https://doi.org/10.1016/j.csbj.2025.12.001
Reference: CSBJ3475

To appear in: *Computational and Structural Biotechnology Journal*

Received date: 9 October 2025
Revised date: 30 November 2025
Accepted date: 1 December 2025

Please cite this article as: Tadas Kraujalis, Lukas Kersys, Andrius Krisciunas, Dalia Calneryte, Auguste Cicinskaite, Lina Kraujaliene, Vytas K. Verselis and Mindaugas Snipas, Model-based Evaluation of Connexin Hemichannel Permeability, *Computational and Structural Biotechnology Journal,* (2025) doi:https://doi.org/10.1016/j.csbj.2025.12.001

Model-based Evaluation of Connexin Hemichannel Permeability

Tadas Kraujalis[1,2], Lukas Kersys[2], Andrius Krisciunas[2], Dalia Calneryte[2], Auguste Cicinskaite[3], Lina Kraujaliene[1], Vytas K. Verselis[4], Mindaugas Snipas[1,3,*]

[1] *Institute of Cardiology at Lithuanian University of Health Sciences, Kaunas, Lithuania*
[2] *Department of Applied Informatics at Kaunas University of Technology, Kaunas, Lithuania*
[3] *Department of Mathematical Modelling at Kaunas University of Technology, Kaunas, Lithuania*
[4] *Dominic P. Purpura Department of Neuroscience, Albert Einstein College of Medicine, New York City, New York, USA*

** Corresponding author: Department of Mathematical Modelling, Faculty of Mathematics and Natural Sciences, Kaunas University of Technology, Studentu str. 50-432, Kaunas LT-51368, Lithuania*
email addresses mindaugas.snipas@ktu.lt   mindaugas.snipas@lsmu.lt

Abstract

Connexin (Cx) hemichannels form intercellular gap junction channels but can also function independently. These large-pore channels are permeable not only to ions but also to small signalling molecules and metabolites. This functional property is relevant to many physiological processes and can be altered by various biochemical factors or disease-causing mutations. In this study, we present a methodology for quantifying and comparing the permeabilities of hemichannels formed by different Cx isoforms using a combination of fluorescence imaging, electrophysiological recordings and mathematical modelling. Fluorescence imaging, coupled with mathematical modelling based on Fick's law and/or the Goldman-Hodgkin-Katz current equation, enables assessment of tracer diffusion rates. These data are integrated with independently obtained electrophysiological measurements of hemichannel activity into a unified statistical model based on the likelihood ratio test. Simulation-based analyses demonstrate that this approach can reliably detect differences as low as two-fold in hemichannel permeability using datasets of moderate size ($n < 100$). Crucially, this approach requires only a minimal amount of time-intensive electrophysiological recording and leverages higher-throughput fluorescence measurements, which can be further streamlined using computational tools for automated cell detection and data extraction. We apply this methodology to compare the permeability of hemichannels formed by wild-type Cx26 and a pore-lining variant, Cx26*A49E. Our results show a significant increase in DAPI permeability in Cx26*A49E hemichannels, consistent with previous findings. This methodology can be extended to assess the permeabilities of other large-pore channels.

Graphical abstract

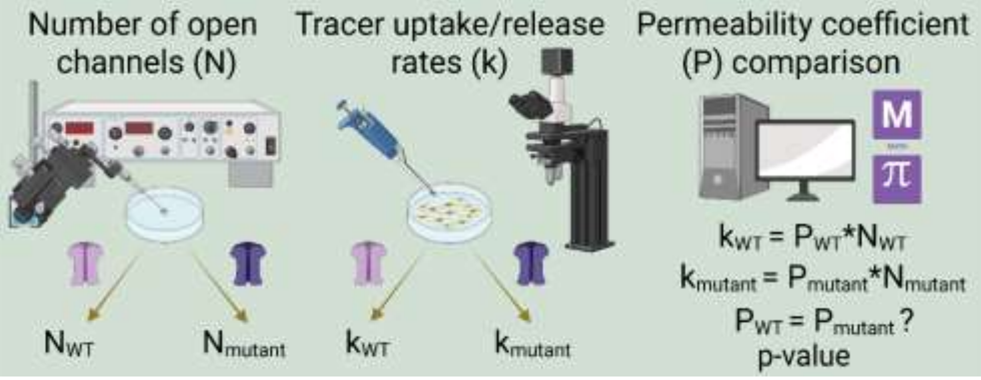

Keywords

Computational modelling, connexin, hemichannel, permeability, electrophysiology, fluorescence imaging

Introduction

Connexin (Cx) proteins form subunits of gap junction (GJ) channels and hemichannels that mediate direct intercellular signalling. GJ channels are formed when two Cx hemichannels, one from each of two neighbouring cells, insert into the plasma membrane and dock in a head-to-head fashion. However, hemichannels were shown to be capable of operating in the absence of docking [1-6], establishing transmembrane signalling as a basic function of Cx proteins. Because of their large pore size, Cx hemichannels allow transmission of a variety of signalling molecules across the plasma membrane. This key functional characteristic of hemichannels has been reported to play physiological and pathological roles in diverse processes such as calcium wave propagation [7], ATP release [8, 9], response to metabolic stress [10, 11], and inflammation [12, 13]. There are 21 different connexins (Cxs) in the human genome that show overlapping, but tissue-specific patterns of expression [14-16]. Although all Cxs form channels with large pores, their unitary conductances have been shown to range over an order of magnitude and are capable of discriminating among permeants on the basis of charge, size and chemical composition (reviewed in [17]). For the most part, these differences have come from studies of GJ channels, but more recent studies in undocked hemichannels indicate a similar range of properties [18-21].

The diversity in Cx hemichannel permeability properties indicates that the nature of the signalling molecules that could be transmitted across the plasma membrane can differ based on the Cx expressed. In addition, Cx channel and hemichannel permeability can be affected by various regulatory factors, such as divalent cations or post-translational modifications [22-26]. Moreover, many disease-causing Cx mutations have been attributed specifically to aberrant hemichannel function. A notable example is syndromic, sensorineural deafness associated with mutations in the Cx26 isoform, and an increased hemichannel open probability and/or altered permeability is a common property of these mutations [27-33]. Importantly, disease-causing syndromic deafness mutations often occur in the NT and E1 domains of Cx26 subunits (reviewed in [34, 35]). These domains constitute the bulk of the Cx pore [36-38], and mutations within them may disrupt cellular function by enhancing passage of harmful molecules and altering the flux of essential signalling molecules.

Electrophysiology provides a direct method for assessing the ionic conductance of Cx hemichannels. In a voltage clamp experiment, the membrane potential is controlled while the resulting ionic currents are recorded. From these currents, macroscopic conductance is obtained using Ohm’s law. Single-channel recordings further resolve discrete current transitions corresponding to the opening or closing of individual (hemi)channels, thereby providing their unitary conductance. Combining whole-cell and single-channel data thus allows an estimate of how many hemichannels are open at a given time. However, electrophysiology reports only the movement of inorganic ions, as permeation of larger charged molecules produces currents that are far too small to detect, and therefore cannot be quantified electrically.

Permeability to larger solutes has therefore been assessed using uptake or leakage assays with fluorescent or radioactive tracers [39, 40]. Tracers of different sizes and charges provide a profile of molecular permeability and can serve as proxies for physiologically relevant permeants. These assays, however, measure only the net accumulation or loss of tracer within the cell and do not directly report the permeability of a single hemichannel. Determining specific hemichannel permeability from such assays requires independent quantification of the number of active hemichannels, typically obtained from electrophysiological recordings. Ideally, electrophysiological and dye flux measurements would be performed simultaneously. In practice, however, concurrent measurements in mammalian cells are difficult because establishing the whole-cell patch clamp configuration disrupts intracellular fluorescence due to dialysis of cellular contents to the pipette. The perforated patch technique can avoid dialysis but is technically challenging, and requires extended recording times to allow for membrane perforation [41]. Moreover, it requires use of high-resistance electrodes that introduces series resistance errors, which is particularly problematic for large conductance channels like Cxs. As a solution, studies have used large Xenopus oocytes to express Cxs and measure tracer flux in conjunction with membrane conductance using a two-electrode voltage clamp and sharp electrodes [21, 42, 43]. Other studies have estimated hemichannel permeability by measuring tracer flux and electrical conductance in the same cells, but not concurrently. For instance, [44] quantified dye uptake in Cx45-expressing HeLa cells, followed by whole-cell patch-clamp recordings of the same cells immediately after dye washout. In [20], hemichannel conductance was first measured in Xenopus oocytes expressing Cx26 or Cx30 using the two-electrode voltage clamp technique, and a subsequent dye release assay was conducted on the same oocytes. While these approaches enable the estimation of both permeability and conductance in the same cells, they are not readily adaptable to high-throughput dye permeability assays.

In this study, we propose a method for assessing and comparing Cx hemichannel permeabilities in mammalian cells that integrates electrophysiological recording, fluorescent imaging, and mathematical/statistical modelling. An advantage of this methodology is that electrophysiological recordings and tracer uptake/release assays are performed separately and then compared using a statistical model. This makes it technically less challenging than approaches that employ electrophysiological recordings and fluorescence imaging in the same cells. Specifically, total and unitary hemichannel conductances are measured to provide estimates of the average number of open hemichannels in a given cell population. In separate cells, fluorescence imaging data from tracer uptake/release assays are combined with mathematical modelling to assess the diffusion rate, which is proportional to the permeability of a single hemichannel. To analyse fluorescence imaging data, we employ machine learning-based cell detection and segmentation, which automates the extraction of fluorescence intensity changes over time. Additionally, it enables cell volume estimation, which is relevant for diffusion rate calculations. The independently obtained conductance and diffusion rate data are then integrated into a statistical model based on the likelihood ratio test. This allows determination of whether hemichannel permeability differs significantly, with associated p-values. Moreover, confidence intervals for permeability differences can be obtained using the profile likelihood technique. Our simulation-based analysis indicates that this methodology can detect permeability differences as small as ~2-fold with moderate sample sizes ($n < 100$).

We demonstrate our methodology using cell cultures expressing WT Cx26 and a Cx26*A49E variant, in which Ala at position 49 is replaced with Glu. Previous studies [19, 45, 46] identified this residue as a key molecular determinant of differential charge permeability characteristics between Cx26 and Cx30 hemichannels. Our results show that Cx26*A49E hemichannels exhibit significantly higher permeability to the positively charged DAPI dye compared to WT channels. This finding aligns with prior studies, further supporting the role of the negatively charged Glu at position 49 as a molecular determinant of Cx26 hemichannel permeability as it relates to the charge of the permeant.

Overall, our study demonstrates that the proposed methodology can be used to effectively compare the permeabilities of different Cx hemichannels. In principle, this approach could be extended to other large-pore channels, such as pannexins, calcium homeostasis regulators (CALHMs), and volume-regulated anion channels (VRACs). A major advantage of this method is that electrophysiological and fluorescent imaging data can be collected separately, allowing for greater experimental flexibility. Moreover, our simulations suggest that increasing sample sizes for either conductance measurements or fluorescence imaging enhances statistical power to a similar extent. Thus, our approach facilitates high-throughput fluorescent imaging, enabling efficient permeability comparisons and reducing the demand for time-intensive electrophysiological recordings.

Methods

Cell Cultures

HeLa mammalian cell lines (ATCC CCL-2) were used for Cx expression. Both wild-type Cx26 and its mutant Cx26*A49E were fused with msfGFP to enable identification of transfected cells. Cell cultures were maintained in Dulbecco‘s Modified Eagle Media (DMEM; Sigma, USA) supplemented with 10 % fetal bovine serum (Sigma, USA) and 1% penicillin-streptomycin solution (10,000 units penicillin and 10 mg/ml streptomycin; Sigma, USA). Cells were incubated under standard conditions of 5% CO_2 at 37 °C. For transient transfection, HeLa cells were transfected on the second day after seeding onto coverslips in Petri dishes using either Lipofectamine 2000 (Invitrogen, USA) or jetPrime (Polyplus Transfection, France) reagents. Experimental procedures were conducted 48 hours post-transfection.

Electrophysiological Recordings

For electrophysiological and fluorescence recordings, HeLa cells grown on glass coverslips were transferred to an experimental chamber mounted on the stage of an Olympus IX70 inverted microscope (Olympus, Japan) equipped with a fluorescence imaging system. Extracellular solution was applied to the bath near the cell using a gravity-driven perfusion system at a flow rate of approximately 2 mL/min. All experiments were conducted at room temperature. Single whole-cell patch-clamp methods were used to record currents from hemichannels using EPC-8 patch-clamp amplifiers (HEKA Elektronik, Germany). Currents were digitized at a sampling rate of 5 kHz and low-pass filtered at 1 kHz. Hemichannel recordings were obtained from voltage steps and ramps applied to single, isolated cells clamped in a whole-cell configuration, which exhibited fluorescent dots in the cell area. Resting membrane potentials were measured using a whole-cell patch-clamp set to a current-clamp mode (with 0 current) immediately after rupturing the seal.

Patch pipettes were fabricated from borosilicate glass tubes with filaments (BF 150-86-10, Sutter Instrument Co., USA) using a P-97 micropipette puller (Sutter Instrument Co., USA) to achieve a resistance of ~3-5 MΩ, minimizing the effects of series resistance on current measurements. For measurements of hemichannel currents, the intracellular solution contained (in mM): 130 CsCl, 10 NaAsp, 0.26 $CaCl_2$, 5 HEPES, 2 BAPTA, and 1 $MgCl_2$, with a pH of 7.7. The divalent-free extracellular solution contained (in mM): 140 NaCl, 4 KCl, 2 CsCl, 1 $BaCl_2$, 5 HEPES, 5 glucose, and 2 pyruvate, with a pH of 7.8. For measurements of resting membrane potentials, CsCl was replaced with KCl.

Data were acquired using AT-MIO-16X D/A boards from National Instruments and analyzed with custom acquisition and analysis software (VTDaq, NexusWiz, written by Brady E. Trexler, Gotham Scientific, Hasbrouck Heights, NJ, USA).

AI-based Cell Detection System for Fluorescence Imaging Experiments

Fluorescent imaging experiments. HeLa cells were grown on glass coverslips, placed in an experimental chamber containing an extracellular solution, and imaged using an Olympus IX70 inverted microscope (Olympus, Japan) equipped with a fluorescence imaging system. Brightfield and fluorescence images were captured using an ORCA digital camera (Hamamatsu, Japan) and processed with UltraVIEW imaging software (PerkinElmer Life Sciences, Boston, MA, USA). Images were acquired with a fixed magnification to ensure consistency across the dataset.

For DAPI (4',6-diamidino-2-phenylindole) uptake experiments, HeLa cells transfected with either wild-type (WT) Cx26 or Cx26*A49E were seeded on glass coverslips and placed on the same setup as described above. The cells were bathed in a divalent-free extracellular solution for 5 minutes to open hemichannels. Subsequently, perfusion with an external solution containing 5 μM DAPI was initiated simultaneously with the start of the recording and maintained at a constant flow rate to ensure a steady supply of the dye throughout the recording period. Bright-field and fluorescence images with EGFP filters were captured for a field of cells prior to DAPI uptake. To monitor DAPI uptake, changes in intracellular fluorescence intensities were recorded every 15 seconds (100 ms exposure time) for the 30-minute recording duration. Appropriate excitation and emission filters were used to visualize DAPI and tagged Cx variants.

Dataset and Annotation. Cell boundary detection was performed using microscopy images of HeLa cells, as detailed in the cell imaging section. Annotation of cell boundaries was done using the online annotation tool provided by makesense.ai. 72 images containing 1 618 cells were used for training and 32 images containing 139 cells for validation. Each image had a resolution of 1 344 × 1 024 pixels, with a pixel size of 0.1075 µm.

Model Architecture and Training. Automated segmentation of cell boundaries was executed using the Detectron2 library, chosen due to its superior segmentation capabilities compared to other advanced methods. The Mask R-CNN architecture with a ResNet-50 backbone combined with a Feature Pyramid Network was applied using the mask_rcnn_R_50_FPN_3x.yaml configuration. The model was trained for up to 4 500 iterations with an initial learning rate set to 0.00025. To improve detection accuracy, a positive Intersection-over-Union (IoU) threshold of 0.5 was used to identify true positives, and a Non-Maximum Suppression threshold of 0.75 was applied to eliminate overlapping detections. Predicted segmentations covering less than 0.3% of the total image area were also excluded to reduce noise. As the dataset contains only a single cell class, the number of classes was set to 1. Training and validation datasets were formatted following the COCO annotation style, and training was carried out on an NVIDIA A100-PCIE-40GB GPU.

Post-processing of Segmentation Results. Post-processing was performed after segmentation to enhance accuracy and consistency. Multi-polygon filtering ensured that each cell was represented by a single continuous segment, retaining only the largest polygon when multiple polygons were produced for one cell. Overlapping segmentations were evaluated using the intersection coefficient (IC), defined as the ratio of the overlapping area to the smaller of the two overlapping areas. Segmentations with an IC greater than 0.5 were resolved by removing the detection with the lower confidence score.

Performance Evaluation. After validation, the model achieved a precision of 75.45% and a recall of 90.65%. Following post-processing, the overall precision improved to 93.94% on the validation dataset, indicating approximately 6% false-positive detections. At the same time, recall reduced to 89.21% compared to 90.65% before filtering, meaning that about 10% of cells were missed during detection. After filtering, the overall accuracy increased from 70.00% to 84.35%. Additionally, the segmentation area accuracy, measured by the IoU between predicted cell boundaries and ground truth, showed an intersection error of less than 1%.

Computations and Statistical Analysis

Mathematical modelling and statistical analyses were implemented in MATLAB. Representative code examples are provided in the Supplementary data. The code for the cell segmentation model is available in a GitHub repository (https://github.com/thr3iog/detectron2-hela-cells-data-extractor), and the annotated data set is deposited in Zenodo (https://zenodo.org/records/17719468).

Results

1. Mathematical model for tracer molecule uptake and release assays

1.1 Changes in concentration of tracer molecule

We begin with a general mathematical model describing the flux of tracer molecules through ion channels expressed in a cell membrane. The rate of concentration change between the cell cytoplasm and extracellular space can be described using a two-compartment model, where diffusion is governed by Fick‘s law. Specifically, the rate of concentration change is proportional to the concentration gradient between the inside and outside of the cell.

Denoting the concentrations of tracer molecules inside and outside the cell at time t as $C_{in}(t)$ and $C_{out}(t)$, respectively, and defining the volumes of the cell and bathing medium as Vol_{in} and Vol_{out}, respectively, the rate of concentration change is governed by the following system of ordinary differential equations (ODEs):

$$\begin{cases} \dfrac{dC_{in}(t)}{dt} = \dfrac{D \cdot \left(C_{out}(t) - C_{in}(t)\right)}{Vol_{in}}; \\ \dfrac{dC_{out}(t)}{dt} = \dfrac{D \cdot \left(C_{in}(t) - C_{out}(t)\right)}{Vol_{out}}. \end{cases} \quad (1)$$

Here variable D represents the diffusion rate constant, which has the dimensions of volume per unit time. Considering a single ion channel type is expressed in the membrane, the diffusion rate constant can also be denoted as the product of the single-channel permeability P (which also has the dimensions of volume per unit time), the number of channels n, and channel open probability p_o:

$$D = P \cdot n \cdot p_o = P \cdot N. \quad (2)$$

Here, $N = n \cdot p_o$ denotes number of open channels. Similarly, the macroscopic channel conductance to ions, g, is the product of the single-channel conductance γ, the number of channels n, and channel open probability p_o:

$$g = \gamma \cdot n \cdot p_o = N \cdot \gamma. \quad (3)$$

This formulation allows the permeability of a single open channel, P, to be evaluated from the relationship

$$P = D/N = D \cdot \gamma / g. \quad (4)$$

Since the volume of the bathing medium is significantly larger than the volume of the cell ($Vol_{out} >> Vol_{in}$) the rate of change in C_{out}, $dC_{out}(t)/dt$, is negligible and can be approximated as zero. Thus, we can assume C_{out} to be constant, $C_{out}(t) = C_{out}$. This assumption simplifies the system of ODEs in Eq. (1) to a single ODE:

$$\frac{dC_{in}(t)}{dt} = \frac{D \cdot \left(C_{out} - C_{in}(t)\right)}{Vol_{in}}. \quad (5)$$

For a tracer uptake assay, the initial concentration of tracer inside a cell is approximately zero, $C_{in}(0) \approx 0$. The solution of Eq. (5) is then given by:

$$C_{in}(t) = C_{out} \cdot \left(1 - \exp\left(-\frac{D}{Vol_{in}} \cdot t\right)\right). \quad (6)$$

The expression is valid when the tracer molecule is electrically neutral or when the membrane potential V_m is at or close to 0. However, many tracer molecules are charged, and cells often maintain significant resting membrane potentials. In such cases, diffusion is also influenced by the electric field across the membrane.

To account for the effects of a transmembrane field, we incorporate the Goldman-Hodgkin-Katz (GHK) current equation, which describes the flux of charged particles under the influence of both concentration and voltage gradients. The modified rate equation becomes:

$$\frac{dC_{in}(t)}{dt} = \frac{D}{Vol_{in}} \cdot \frac{z \cdot F \cdot V_m}{R \cdot T} \cdot \frac{\left(C_{out} \cdot \exp\left(-\frac{z \cdot F \cdot V_m}{R \cdot T}\right) - C_{in}(t)\right)}{\left(1 - \exp\left(-\frac{z \cdot F \cdot V_m}{R \cdot T}\right)\right)}. \tag{7}$$

Here *z* is the valence of the tracer molecule, *F* is Faraday's constant, *R* is the gas constant, and *T* is an absolute temperature.

For convenience, we define a dimensionless parameter $\mu = (z \cdot F \cdot V_m)/(R \cdot T)$, the effective diffusion rate constant $D^* = D \cdot \mu/(1 - \exp(-\mu))$, and the effective external concentration $C^*_{out} = C_{out} \cdot \exp(-\mu)$. Using these definitions, Eq. (7) can be rewritten in a form analogous to Eq. (5):

$$\frac{dC_{in}(t)}{dt} = \frac{D^* \cdot \left(C^*_{out} - C_{in}(t)\right)}{Vol_{in}}. \tag{8}$$

The solution of this equation is structurally similar to Eq. (6):

$$C_{in}(t) = C^*_{out} \cdot \left(1 - \exp\left(-\frac{D^*}{V_{in}} \cdot t\right)\right). \tag{9}$$

For uncharged tracer molecules (z = 0) or when the membrane potential is zero ($V_m = 0$), the dimensionless parameter μ is also 0. By applying l'Hopital's Rule, it can be shown that $\mu/(1 - \exp(-\mu))$ approaches 1 when μ approaches 0, reducing Eq. (7) to the original Fick's law-based formulation in Eq. (5).

The ODEs in Eq. (1) can also be adapted to describe intracellular concentration changes during dye release assays. In this case, the concentration of the tracer molecule in the bathing medium remains effectively zero due to its much larger volume relative to the cell. Consequently, the dynamics of $C_{in}(t)$ are governed by:

$$\frac{dC_{in}(t)}{dt} = -\frac{D \cdot C_{in}(t)}{Vol_{in}}. \tag{10}$$

The solution to this equation describes an exponential decay of intracellular tracer concentration from the initial value $C_{in}(0)$ towards zero:

$$C_{in}(t) = C_{in}(0) \cdot \exp\left(-\frac{D}{Vol_{in}} \cdot t\right). \tag{11}$$

For charged tracer molecules, this model can be further extended to account for the influence of the resting membrane potential using the GHK formulations. Similar to the dye uptake model, this is achieved by replacing *D* in Eq. (11) with the effective diffusion rate constant $D^* = D \cdot \mu/(1 - \exp(-\mu))$, where μ incorporates the effects of the membrane potential as previously defined.

1.2 Relationship between changes in concentration and fluorescence intensity

Under experimental conditions, the concentration *C*(*t*) is assessed from the fluorescence intensity, *F*(*t*), which for many tracers depends linearly on the concentration with the ranges used [47, 48]. Thus, *F*(*t*), can be described by the following relationship:

$$F(t) = f \cdot C(t) + F_0. \tag{12}$$

Here f is a constant denoting fluorescence per unit concentration, and F_0 is the background fluorescence, representing the fluorescence in the absence of tracer molecules. Both $F(t)$ and F_0 are measured in artificial units ($a.\ u.$).

Thus, in a tracer uptake assay, the increase in fluorescence intensity inside a cell, $F_{\mathrm{in}}(t)$, is given by:

$$F_{in}(t) = f \cdot C_{out}^{*} \cdot \left(1 - \exp\left(-\frac{D^{*}}{Vol_{in}} \cdot t\right)\right) + F_0. \tag{13}$$

The background fluorescence can be measured at the beginning of the tracer uptake experiment, when $C_{in}(t)$ is equal to zero:

$$F_{in}(0) = f \cdot C_{in}(0) + F_0 = F_0. \tag{14}$$

By subtracting the background fluorescence and normalizing to the initial fluorescence level, we obtain the following relationship:

$$F_{norm}(t) = \frac{F_{in}(t) - F_{in}(0)}{F_{in}(0)} = \frac{f \cdot C_{out}^{*}}{F_0} \cdot \left(1 - \exp\left(-\frac{D^{*}}{V_{in}} \cdot t\right)\right). \tag{15}$$

For tracer release assays described by Eq. (11), a very similar expression to Eq. (15) can be obtained by considering background-subtracted fluorescent recordings $F_{in}(0) - F_{in}(t)$. More precisely, it has the following form:

$$F_{in}(0) - F_{in}(t) = f \cdot C_{in}(0) \cdot \left(1 - \exp\left(-\frac{D^{*}}{V_{in}} \cdot t\right)\right). \tag{16}$$

1.3 Fitting mathematical model to experimental data

Equations (15) and (16) predict that the normalized and/or background-subtracted changes in fluorescence intensity obtained in tracer uptake and release assays can be well described by an exponential function of the form

$$f(t) = a \cdot (1 - \exp(-b \cdot t)). \tag{17}$$

where parameter a corresponds to $f \cdot C_{out}^{*}/F_0$ or $f \cdot C_{out}^{*}$, and b reflects the effective diffusion rate per unit cell volume, D^{*}/Vol_{in}. This function predicts the saturation of normalized fluorescence intensity as the concentration of tracer inside the cell, $C_{in}(t)$, approaches that of the bathing medium, C_{out}.

When the effective diffusion rate is low, $F_{norm}(t)$ is far from saturation. Thus, the early kinetics of $F_{norm}(t)$ can be described by a linear function. This behaviour can be modelled by approximating the right-hand side of Eq. (15) using the first-order Taylor series expansion of the exponential function around zero, $e^{\pm x} \approx 1 \pm x$, which is valid for sufficiently small values of x. Under this approximation, $F_{norm}(t)$ can be expressed as:

$$F_{norm}(t) = \frac{F_{in}(t) - F_{in}(0)}{F_{in}(0)} = \frac{f \cdot C_{out}^{*} \cdot D^{*}}{F_0 \cdot Vol_{in}} \cdot t. \tag{18}$$

A very similar expression can be obtained by applying the Taylor series expansion for background-subtracted recordings from tracer release assays, presented in Eq. (16):

$$F_{in}(0) - F_{in}(t) = \frac{f \cdot C_{in}(0) \cdot D^{*}}{Vol_{in}} \cdot t. \tag{19}$$

Thus, Eqs. (18)-(19) predict that the normalized and/or background-subtracted fluorescence intensity in tracer uptake and release assays initially follows a linear relationship of the form:

$$f(t) = k \cdot t. \tag{20}$$

A representative example of a DAPI uptake experiment in cells transfected with Cx26 is shown in Fig. 1A. Control experiments in untransfected HeLa cells did not show significant DAPI uptake (Fig. 1B).

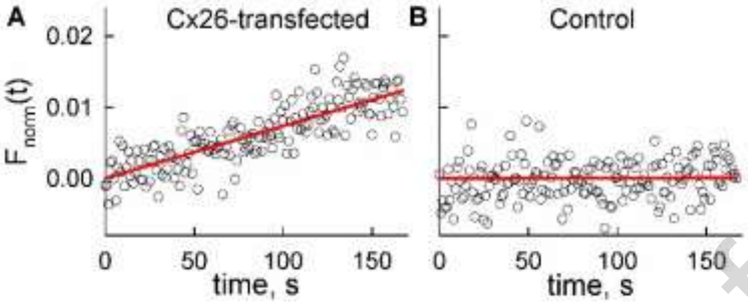

Fig. 1. Representative examples of changes in normalized intracellular fluorescence intensity, $F_{norm}(t)$, during a DAPI permeation assay. **(A)** Cx26-transfected cells show visible uptake of DAPI. At the initial phase of the experiment, the recorded signal (open black circles) shows no indication of saturation and is well-fitted by a linear function $F_{norm}(t) = k \cdot t$ with slope $k = 7.38 \cdot 10^{-5}$ s^{-1} significantly different from 0 (p-value < 0.0001). (**B**) Control experiments in untransfected cells did not show significant uptake of DAPI. In this case, slope $k = 5.23 \cdot 10^{-7}$ s^{-1} of the fitted linear function $F_{norm}(t) = k \cdot t$ was not significantly different from 0 (p-value 0.8130).

In Eq. (20), the slope k reflects the quantity $(f \cdot C^*_{out} \cdot D^*)/(F_0 \cdot Vol_{in})$ or $(f \cdot C_{in}(0) \cdot D^*)/Vol_{in}$, which has the dimension of a rate or a rate multiplied by fluorescence intensity, respectively. Importantly, the slope k can be directly compared to the product $a{\cdot}b$ from the exponential function $f(t) = a{\cdot}(1 - exp(-b{\cdot}t))$, as both k and $a{\cdot}b$ describe the same physical quantity. However, this comparison is valid only when the saturation of $F_{norm}(t)$ is determined primarily by diffusion. In certain cases, such as with DAPI, which fluoresces upon binding to nucleic acids, saturation may instead be limited by the availability of binding sites rather than diffusion. To avoid this confounding factor, our analysis focuses only on the initial linear segments of the data.

Thus, using a kinetic model to describe changes in fluorescence intensity in tracer uptake assays allows us to estimate the parameter $k = (f \cdot C^*_{out} \cdot D^*)/(F_0 \cdot Vol_{in})$. Using previous definitions for C^*_{out} and D^*, as well as Eqs. (2)-(4), k can be expressed as follows:

$$k = \left(\frac{f \cdot C_{out}}{F_0}\right) \cdot \left(\frac{\mu \cdot \exp(-\mu)}{1 - \exp(-\mu)}\right) \cdot \left(\frac{P \cdot N}{Vol_{in}}\right). \tag{21}$$

Here the initial fluorescence background level, F_0, is directly obtained from imaging experiments, as is the concentration of tracer molecules in the bathing medium, C_{out}. Parameter $\mu = \frac{(z \cdot F \cdot V_m)}{(R \cdot T)}$ depends on resting membrane potential V_m, which can be evaluated from independent electrophysiological recordings. Thus, we can define the estimable quantity K

$$K = k \cdot \left(\frac{F_0}{C_{out}}\right) \cdot \left(\frac{1 - \exp(-\mu)}{\mu \cdot \exp(-\mu)}\right) = \frac{f \cdot P \cdot N}{Vol_{in}}. \tag{22}$$

The quantity K has units of fluorescence intensity per concentration per time. For tracer release assays, the equivalent expression for K can be obtained by removing F_0 and replacing C_{out} with $C_{in}(0)$. The relative fluorescence intensity per concentration unit, f, in principle, cannot be easily determined during a tracer uptake experiment, as it depends not only on the properties of the fluorophore but also on experimental conditions. However, if the same conditions are maintained across different imaging experiments, f can be assumed constant, as it should not depend on the type of permeable channels. Consequently, the estimated quantity K should be proportional to the product of single-channel permeability P and total conductance g, and inversely proportional to cell volume Vol_{in}.

2. Cell segmentation and fluorescence imaging data extraction using computer vision

Automated imaging and detection systems based on artificial intelligence and deep learning are increasingly used in cellular and molecular imaging to increase throughput and reproducibility [49]. Such techniques have been successfully applied to tasks including cell segmentation, phenotypic classification and particle localization [50-52]. In this study, we employed a deep learning-based cell detection system for automated segmentation of HeLa cell boundaries (detailed in Methods section). This approach enabled automatic extraction of fluorescence intensity dynamics, as well as estimation of cell surface area and cell volume for the dye uptake experiments.

First, the bright-field images were analysed by the segmentation model to identify individual cell boundaries (see a representative example in Fig. 2A and B). Following the segmentation, cell boundaries from bright-field images were overlapped onto fluorescence dark-field images acquired using EGFP filter sets to visualize Cx26 or Cx26*A49E expression. To evaluate Cx expression levels, we quantified the average pixel intensity within each automatically segmented cell region. Cells with mean fluorescence intensities above a defined threshold were considered to be positive for Cx expression (transfected) and were highlighted with green boundaries. In contrast, cells that did not exhibit significant fluorescence, were deemed as untransfected and were highlighted with red boundaries (Fig. 2C).

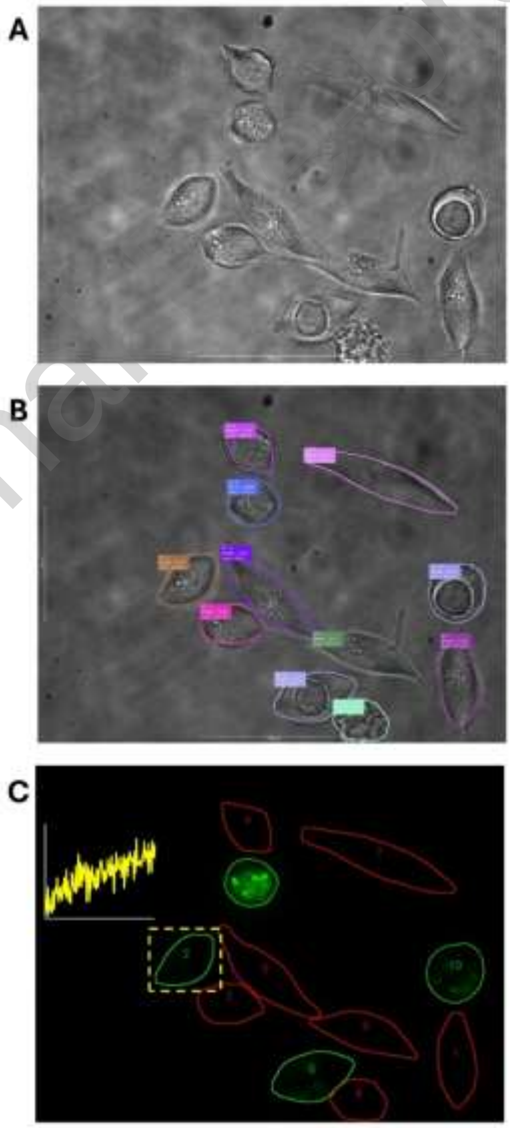

Fig. 2. Automated cell segmentation and quantification of dye uptake in connexin-expressing HeLa cells. (A) A fragment of a representative bright-field image used to identify cell boundaries. **(B)** The same bright-field image as in (A), but with identified cell boundaries, denoted by solid lines of different colours.

Cell segmentation was performed using a deep learning-based Mask R-CNN model. Additional cell parameters, enabled by cell identification, such as surface area measurements are shown next to individual cells. **(C)** Fluorescence dark-field image showing Cx expression, which was obtained using EGFP filter sets. Cells with mean fluorescence intensity above a set threshold, indicating Cx expression, are highlighted in green, while untransfected cells are outlined in red. The yellow curve represents the time course of DAPI uptake within the marked cell region (yellow dashed rectangle).

Subsequent analysis focused on Cx-expressing cells. DAPI uptake was evaluated by calculating the change in the average pixel intensity within each defined cell boundary over time. Fig. 2C shows a representative example of fluorescence changes over time (solid yellow line in a graph) extracted from the Cx-expressing cell denoted by the dashed rectangular region.

3. The relationship between Cx hemichannel conductance and fluorescence intensity of msGFP inside segmented cells

First, we examined whether the fluorescence intensity of a cell expressing an msGFP-tagged Cx protein could serve as a proxy for the number of functional Cx hemichannels. If successful, this approach could significantly reduce the need for time-consuming electrophysiological measurements, thereby streamlining data analysis.

To evaluate the relationship between fluorescence intensity and hemichannel conductance, we performed whole-cell patch-clamp recordings on single, isolated cells. To promote hemichannel opening and prevent their inhibition by extracellular divalent cations, cells were incubated for five minutes in a divalent cation-free solution, which was also used for continuous perfusion during the recording. Hemichannel currents were measured at the onset of a voltage step, providing an estimate of hemichannel conductance, g. Dividing this overall conductance by the unitary conductance γ yielded an estimate of the number of open Cx hemichannels, g/γ, at a given time.

Simultaneously, we captured bright-field and dark-field images of each cell. Bright-field images were used for deep learning-based cell boundary detection. The dark-field images were excited using EGFP filters, which allowed us to assess Cx protein expression inside the cell (see a representative example in Fig. 3A). Expression levels were assessed by summing the pixel intensities within the segmented cell boundaries, which provides the total msGFP fluorescence intensity (FI_{msGFP}). This procedure allowed examination of the relationship between FI_{msGFP} and number of open hemichannels.

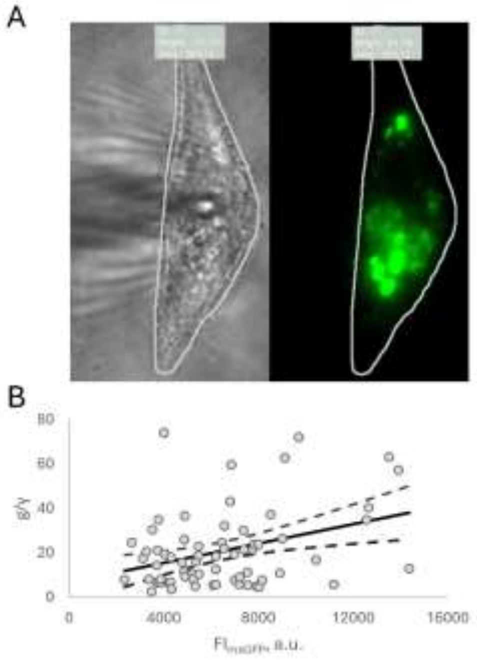

Fig 3. The number of open Cx hemichannels in cell membrane is not reliably predicted by the total cellular fluorescence intensity. (A) Representative images of a cell expressing WT Cx26-msGFP protein. Left panel shows bright-field image displaying cellular morphology. Right panel presents fluorescence image indicating Cx26-msGFP protein expression. The cell boundary (white contour line) was obtained using a deep learning-based segmentation model. **(B)** The relationship between fluorescence of msGFP protein, FI_{msGFP}, and the ratio of overall and unitary Cx hemichannel conductances, which reflects the number of functional Cx hemichannels in a cell. Solid line represents a best-fit linear model, while dashed lines show 95 % confidence intervals.

Fig. 3B shows the g/γ-FI_{msGFP} relationship in cells expressing either WT Cx26 or the mutant Cx26*A49E. Visual inspection reveals a weak to moderate linear correlation between g/γ and FI_{msGFP}, which was confirmed by a statistically significant but relatively low Pearson correlation coefficient ($\rho = 0.35$, p-value = 0.0036). Most notably, the coefficient of determination for a fitted linear model was very low ($R^2 = 0.125$), indicating that only ~12.5 % of the variance in functional channel number can be explained by fluorescence intensity. In addition, a substantial fraction of data points lies outside the 95 % confidence intervals of the fitted model (dashed lines in Fig. 3B). Together, these findings strongly suggest that FI_{msGFP} is not a reliable proxy for the number of open hemichannels, and that direct electrophysiological measurements remain necessary.

This result is not unexpected as total cellular fluorescence reflects not only functional, membrane-inserted Cx hemichannels but also non-functional pools, such as misfolded subunits, proteins undergoing trafficking, and channels targeted for degradation. Additionally, even membrane-localized Cx might be non-conducting due to gating state or post-translational modifications.

4. Evaluation of cell volume using data from cell segmentation and imaging system

To quantify fluorescence intensity changes during tracer uptake assays, we employed a kinetic ODE model in which the parameter $K = (f \cdot P \cdot N)/Vol_{in}$ represents a composite rate constant. Here f denotes fluorescence per unit of concentration, P is single-channel permeability, N is the number of open channels, and Vol_{in} is the intracellular volume. Although a number of previous studies assign a constant value to cell volume [53] or assumed that it is unaffected by the type of expressed channels [19], we sought to explicitly evaluate Vol_{in} and its influence on the assessment of Cx hemichannel permeability in individual cells.

Accurate cell volume measurements logically require imaging techniques that provide 3D rendering. However, adherent cells grown on glass coverslips, like those used in our DAPI uptake assay, typically spread over the coverslip surface. Thus, their shape can be approximated by a prism with an irregular base. Under this assumption, Vol_{in} can be estimated based on the cell surface area A_{in} obtained from fluorescent imaging segmentation:

$$Vol_{in} = A_{in} \cdot h, \tag{23}$$

where h is the average cell height.

Real cell morphology is complex, with height varying across the cell. For example, HeLa cells can range from submicron heights near the periphery to ~4.5 μm at the center [54]. However, using an average height provides a practical approximation. Therefore, even if local height varies, the total volume should scale proportionally with the measured surface area.

Using our cell segmentation data, we calculated surface areas and estimated Vol_{in}, assuming an average cell height of ~3 μm based on measurements presented in [54]. Because the segmentation model exhibits approximately 5-10 % error in estimating the projected cell area A_{in}, Eq. (23) implies a corresponding 5-10 % uncertainty in Vol_{in} estimation. Furthermore, since $K = C/Vol_{in}$, where C is a constant, an error of up to 10 % in Vol_{in} propagates to approximately 9-11 % error in the estimated rate parameter K.

To evaluate the relevance of these estimates for permeability analyses, we examined the relationship between Vol_{in}, the rate parameter K, and the single-channel permeability P using a statistical model, which is presented in the following section.

5. Statistical test for comparing permeabilities of different channels using fluorescent imaging and electrophysiological data

Fluorescence imaging provides an estimable quantity K, which is proportional to the product of single-channel permeability P and total conductance g. If the total conductance, g, is not measured simultaneously with fluorescence imaging data, direct comparison of estimated values of K does not necessarily reveal differences in P, as variations in K may also reflect differences in the number of open channels. Thus, for a direct comparison of single-channel permeability, it is necessary to separate differences in overall diffusion rates from the number of open channels. We propose that this can be achieved through statistical modelling given that single-channel permeability, P, is a constant for a given channel type across experiments. The estimated number of open channels, N, can vary significantly between experiments and is treated as a random variable. To determine differences in single-channel permeability P from estimates of the quantity K, we propose a statistical strategy that requires incorporating independent electrophysiological measurements of N. The measurements should be obtained under the same conditions used in the fluorescent imaging experiments. Additionally, the same cell lines should be used to minimize variability caused by potential cell-specific differences in expression, as well as differences in channel properties produced by cytosolic factors.

Challenges in direct comparison of Cx channel permeabilities. In our direct comparison of the permeabilities, we assume wild-type (WT) and mutant channels. To compare their permeabilities, designated as P_{wt} and P_{mut}, respectively, we incorporate independent datasets for functional hemichannel measurements (N_{wt} and N_{mut}) along with the estimated K values (K_{wt} and K_{mut}).

1) Assumption of identical conductance distributions: If N_{wt} and N_{mut} follow the same distribution, direct comparison of K_{wt} and K_{mut} would be valid, as any observed difference would reflect a difference in P_{wt} and P_{mut}. However, this approach requires two consecutive statistical tests – first, to compare the distribution of N_{wt} and N_{mut}, and second, to compare K_{wt} and K_{mut}. This increases the probability of false positives or negatives. Thus, the p-values in these two steps should be adjusted accordingly. For example, for an overall significance level of 0.05, each individual test should use $1 - \sqrt{1 - 0.05} \approx 0.0253$.

2) Differences in conductance distributions: If N_{wt} and N_{mut} differ significantly (e.g., due to altered open state probability, expression levels, or trafficking of mutant channels), direct comparison of K_{wt} and K_{mut} is problematic. If N_{wt} is systematically higher than N_{mut}, higher mean values of K_{wt} do not necessarily imply that P_{wt} is greater than P_{mut}. To address these limitations, we propose a statistical model based on the likelihood ratio test.

Likelihood ratio test for channel permeability. The likelihood ratio test evaluates whether a more complex model provides a significantly better fit to the data than a simpler model, which is a special case (submodel) of the expanded model. The submodel has fewer parameters and necessarily provides a lower likelihood estimate. However, if the likelihood gain from the expanded model is insignificant, the simpler model is preferred. This can be quantified using the ratio of likelihoods:

$$\lambda = -2 \ln \left(\frac{L_{submodel}}{L_{expanded}} \right). \tag{24}$$

Under the null hypothesis (i.e., the submodel fits data as well as the expanded model), λ follows a chi-squared distribution with degrees of freedom equal to the difference in parameter count between the models.

Formulation of the model. Since K_{wt} is proportional to N_{wt}, we express it as $K_{wt} = C_{wt} \cdot N_{wt}$, where C_{wt} is assumed to be a constant, reflecting single-channel permeability. Similarly, for mutant channels $K_{mut} = C_{mut} \cdot N_{mut}$.

If N_{wt} follows a probability distribution with a cumulative distribution function $F_{wt}(x; \theta_{wt,1}, \cdots, \theta_{wt,m})$, then K_{wt} follows a probability distribution with a cumulative distribution function $F_{wt}(x/C_{wt}\, ; \theta_{wt,1}, \cdots, \theta_{wt,m})$. Similarly, for N_{mut} and K_{mut} the respective cumulative distribution functions are given by $F_{mut}(x; \theta_{mut,1}, \cdots, \theta_{mut,n})$ and $F_{mut}(x/C_{mut}\, ; \theta_{mut,1}, \cdots, \theta_{mut,n})$. If N_{wt} and N_{mut} follows the same type of distribution, they would have the same number of parameters (e.g., $m = n$), although their values may differ.

Many common distributions, such as the gamma distribution, are stable under multiplication by a constant, preserving the functional form of K. For example, if $X \sim G(\alpha, \sigma)$ (gamma-distributed with shape parameter α and scale parameter σ), then multiplying X by a positive constant C results in another gamma-distributed random variable with the same shape parameter α, and scale parameter $C\cdot\sigma$: $Y \sim G(\alpha, C \cdot \sigma)$. Thus, if $N_{wt} \sim G(\alpha_{wt}, \sigma_{wt})$, then $K_{wt} \sim G(\alpha_{wt}, C_{wt} \cdot \sigma_{wt})$, preserving the distribution type.

Maximum likelihood estimation. We define the submodel under the null hypothesis that assumes equal permeabilities:

- $N_{wt} \sim F_{wt}(x; \theta_{wt,1}, \cdots, \theta_{wt,m})$;
- $K_{wt} \sim F_{wt}(x/C_{wt}\, ; \theta_{wt,1}, \cdots, \theta_{wt,m})$;
- $N_{mut} \sim F_{mut}(x; \theta_{mut,1}, \cdots, \theta_{mut,m})$;
- $K_{mut} \sim F_{mut}(x/C_{mut}\, ; \theta_{mut,1}, \cdots, \theta_{mut,m})$;
- $C_{wt} = C_{mut} = C$ (assuming equal permeability)

The model has $2m + 1$ parameters, assuming the same type of distributions for g_{wt} and g_{mut}. In the expanded model, the assumption $C_{wt} = C_{mut} = C$ is removed, allowing for different permeabilities between WT and mutant channels. Thus, the expanded model has $2m + 2$ parameters.

After estimating likelihood $L_{submodel}$ and $L_{expanded}$, we compute $\lambda = -2 \ln\left(\frac{L_{submodel}}{L_{expanded}}\right) \sim \chi^2(1)$. Under the null hypothesis, p-value is given by: $p = 1 - F_{\chi^2}(\lambda; 1)$. If $p < 0.05$, we reject the null hypothesis, indicating significant difference in permeabilities.

Construction of confidence intervals based on profile likelihood. The likelihood ratio test can be extended to estimate the ratio of permeability constants, $R = C_{mut}/C_{wt}$, and its confidence interval using the profile likelihood technique. In this case, the submodel assumption $C_{wt} = C_{mut} = C$ is replaced by a more general form

- $C_{mut} = R \cdot C_{wt}$

where R is treated as a fixed value. For each tested value of R, we maximize likelihood of the constrained model, obtaining $L_{submodel}(R)$, and then compute $\lambda(R) = -2 \ln\left(\frac{L_{submodel}(R)}{L_{expanded}}\right)$. The 95 % confidence interval for R is defined as the set of all R values satisfying inequality $p(R) = 1 - F_{\chi^2}(\lambda(R); 1) > 0.05$. Thus, the smallest and largest values of R for which this inequality still holds give us the lower and upper bounds of the 95 % confidence interval.

Model validation. To ensure the validity of the model, the estimated parameters should fit empirical data well. This can be assessed using standard nonparametric tests, such as the Kolmogorov-Smirnov test, to compare the observed data distributions with those predicted by the model.

Evaluation of cell volume data. In our proposed model, the composite rate parameter $K = (f \cdot P \cdot N)/Vol_{in}$ is assumed to be proportional to *N*, other factors being constant. That is, $K = C \cdot N$, with constant *C*. However, Vol_{in} varies across individual traces, even within the same cell line. If not accounted for, this variation may introduce additional noise, leading to discrepancies from the assumed relationship $K = C \cdot N$. This in turn constrains the joint distribution of *N* and *K* – for example, to the same distribution family such as gamma. We propose that the statistical model can also serve as a tool to assess the quality of surface-area-based estimates of Vol_{in}. If these estimates reflect true cell volumes, then incorporating Vol_{in} into the model should improve the fit. Specifically, if replacing the *K* data sets with $K \cdot Vol_{in}$ improves goodness-of-fit, this would support the validity and informativeness of the obtained Vol_{in} estimates.

6. Application of the proposed methodology to experimental data

We applied the proposed methodology to electrophysiological and fluorescence imaging data obtained from DAPI uptake assays in hemichannels formed by WT Cx26 and the Cx26*A49E variant. The charge at position 49 in Cx26 was shown to influence permeability of tracer based on charge and to account for the different permeability characteristics of Cx26 and Cx30 GJ channels and hemichannels [19].

First, we measured the total conductance of WT Cx26 and Cx26*A49E hemichannels using whole-cell patch-clamp recordings. These measurements were performed near 0 mV membrane voltage in divalent cation-free solutions to replicate the conditions used in DAPI uptake assays. A unitary conductance of ~340 pS was used, as reported in [55]. Dividing the measured conductance by unitary conductance, g/γ, gave us the estimates of open hemichannels, *N*. In total, we obtained 40 measurements of *N* for WT Cx26 and 40 for Cx26*A49E hemichannels.

In DAPI uptake assays, we recorded the changes of fluorescence intensity over time. Each background-subtracted and normalized time course was fitted using the proposed kinetic model. For each time course, linear fits described in Eqs. (18) and (20) yielded the rate parameter *K*, defined in Eq. (22). In total, we obtained 70 estimates of *K* for WT Cx26 and 36 for Cx26*A49E hemichannels. Experimentally measured resting membrane potential in Cx-transfected cells was close to zero, with a small standard deviation (V_m = -7.91 ± 1.28 mV, *n* = 15) and no significant differences between WT Cx26 and Cx26*A49E transfected cells (p-value 0.479). Model predictions indicate that variation of this magnitude introduce relatively small (less than 10 %) changes in the estimated rate parameters *K* (see Supplementary Figure S1). Additionally, because these deviations affect WT and Cx26*A49E recordings similarly, they do not influence the comparison of relative permeabilities.

To analyse the datasets N_{Cx26}, $N_{Cx26*A49E}$, K_{Cx26}, and $K_{Cx26*A49E}$, we applied the proposed statistical model based on the likelihood ratio test. Several candidate distributions available in the MATLAB Statistics and Machine Learning Toolbox were fitted to each dataset independently. The gamma distribution provided the best fits and was therefore selected for subsequent analyses.

In the restricted submodel, the permeability constants of Cx26 and Cx26*A49E, denoted as C_{Cx26} and $C_{Cx26*A49E}$, were assumed to be equal, leading to the following five-parameter submodel:

- $N_{Cx26} \sim G(x; \alpha_{Cx26}, \sigma_{Cx26});$
- $K_{Cx26} \sim G(x/C_{Cx26}\,; \alpha_{Cx26}, \sigma_{Cx26});$
- $N_{Cx26*A49E} \sim G(x; \alpha_{Cx26*A49E}, \sigma_{Cx26*A49E});$
- $K_{Cx26*A49E} \sim G(x/C_{Cx26*A49E}\,; \alpha_{Cx26*A49E}, \sigma_{Cx26*A49E});$
- $C_{Cx26} = C_{Cx26*A49E} = C.$

In contrast, the expanded model allowed for permeability coefficients to differ from each other. Thus, eliminating the condition $C_{Cx26} = C_{Cx26*A49E} = C$ resulted in a six-parameter statistical model. These models were fit to the data using the maximum likelihood criterion.

To test the validity of the surface-area-based cell volume estimates, we also evaluated volume-adjusted permeability values, $K \cdot Vol_{in}$. For the Cx26*A49E hemichannels, two outliers were excluded from the obtained $K\cdot Vol_{in}$ data set using a conservative criterion of six median absolute deviations from the median. Estimated parameters and corresponding log-likelihoods (LLs) are shown in Table 1.

Table 1. Estimated parameters of statistical models.

	N and K		N and $K\cdot Vol_{in}$	
	$C_{Cx26} = C_{Cx26*A49E}$	$C_{Cx26} \neq C_{Cx26*A49E}$	$C_{Cx26} = C_{Cx26*A49E}$	$C_{Cx26} \neq C_{Cx26*A49E}$
α_{Cx26}	2.8806	3.1398	2.1386	2.4048
σ_{Cx26}	5.8297	6.6420	7.3229	8.6720
C_{Cx26}	0.000133	0.000093	0.2069	0.1259
$\alpha_{Cx26*A49E}$	1.0103	2.3829	1.3703	2.3104
$\sigma_{Cx26*A49E}$	55.5155	7.3041	26.3297	7.5335
$C_{Cx26*A49E}$	0.000133	0.000759	0.2069	0.6899
LL	169.39	213.91	-571.08	-540.93

Likelihood ratio tests yielded a statistic $\lambda = 89.04$ using the N and K datasets, and $\lambda = 60.30$ when using N and the volume-adjusted quantity $K\cdot Vol_{in}$. In both cases, the corresponding p-values were effectively 0, indicating that the expanded model, which allows distinct permeabilities for WT Cx26 and Cx26*A49E, provides a significantly better fit than the restricted model with equal permeabilities. We also performed a profile likelihood analysis to obtain 95 % confidence intervals for the permeability ratio between Cx26*A49E and WT Cx26 hemichannels. For the volume-adjusted dataset, the analysis indicated that Cx26*A49E hemichannels are between 3.71-fold and 8.14-fold more permeable than WT. For the non-adjusted dataset, the corresponding 95% confidence interval was 5.69-fold to 11.85-fold. Analysis using alternative distributions, for example, Weibull instead of gamma, yielded highly similar 3.60- to 7.77-fold ratio for the volume-adjusted data and 5.81- to 11.75-fold for the non-adjusted datasets. This indicates that the inferred permeability differences are not sensitive to the choice of distribution.

Further validation was performed using Kolmogorov-Smirnov test. The p-values obtained for the gamma distribution fits are listed in Table 2.

Table 2. Kolmogorov-Smirnov test p-values.

Dataset	$C_{Cx26} = C_{Cx26*A49E}$	$C_{Cx26} \neq C_{Cx26*A49E}$
N_{Cx26}	0.3498	0.1811
K_{Cx26}	0.0880	0.7234
$N_{Cx26*A49E}$	$5.26\cdot 10^{-6}$	0.6905

$K_{Cx26*A49E}$	$2.53 \cdot 10^{-7}$	0.2326
N_{Cx26}	0.1049	0.4968
$K_{Cx26} \cdot Vol_{in}$	0.0014	0.8495
$N_{Cx26*A49E}$	0.0028	0.7130
$K_{Cx26*A49E} \cdot Vol_{in}$	$4.20 \cdot 10^{-12}$	0.6336

The Kolmogorov-Smirnov test results clearly show that the expanded model, which allows different permeability constants, provides substantially better fits. For the expanded model, all p-values exceeded 0.05, indicating adequate agreement with the data. In contrast, the restricted model exceeded this threshold only for the unadjusted K values in the Cx26 datasets and for N_{Cx26} when combined with volume-adjusted $K \cdot Vol_{in}$.

Furthermore, volume-adjusted $K \cdot Vol_{in}$ values yielded higher p-values across datasets, indicating better model fits. They also produced lower AIC values for both N_{Cx26} and $N_{Cx26*A49E}$ datasets (K and $K \cdot Vol_{in}$ datasets do not allow for direct comparison due to different scales). For example, using unadjusted K, AIC values were 499.46 and 368.91, whereas with volume-adjusted data, they were only 394.35 and 359.26; differences greater than 2 units are considered statistically significant, lower values indicating better fit. Thus, the improved fits suggest that the volume-adjusted variable $K \cdot Vol_{in}$ more accurately preserves the expected distribution, as predicted by the relationships $K \cdot Vol_{in} = C \cdot N$, compared to the unadjusted K values predicted by $K = C \cdot N$. This supports the hypothesis that surface-area-based Vol_{in} estimates are informative proxies for actual cell volumes.

The theoretical cumulative distribution function fits are presented in Fig. 4. Overall, these results demonstrate that WT Cx26 and Cx26*A49E hemichannels exhibit significantly different permeabilities to DAPI. The expanded model predicts that Cx26*A49E hemichannels are more permeable, showing statistically significant ~3- to ~11-fold increase in estimated permeability coefficient. This finding is consistent with previous studies indicating that the negatively charged ring near position 49 is critical for permeability in Cx26 and Cx30 hemichannels [46, 55]. The neutral-to-negative substitution at this site enhances Cx26 permeability to positively charged molecules such as DAPI. Permeability differences of comparable magnitude have also been reported for Cx26 mutations associated with syndromic deafness. For example, Cx26*T8M and Cx26*N206S channels exhibited an ~3.5-fold reduction in permeability to ethidium bromide [32], whereas the Cx26*G45E hemichannels showed a marked increase in Ca^{2+} permeability compared to WT Cx26 [56].

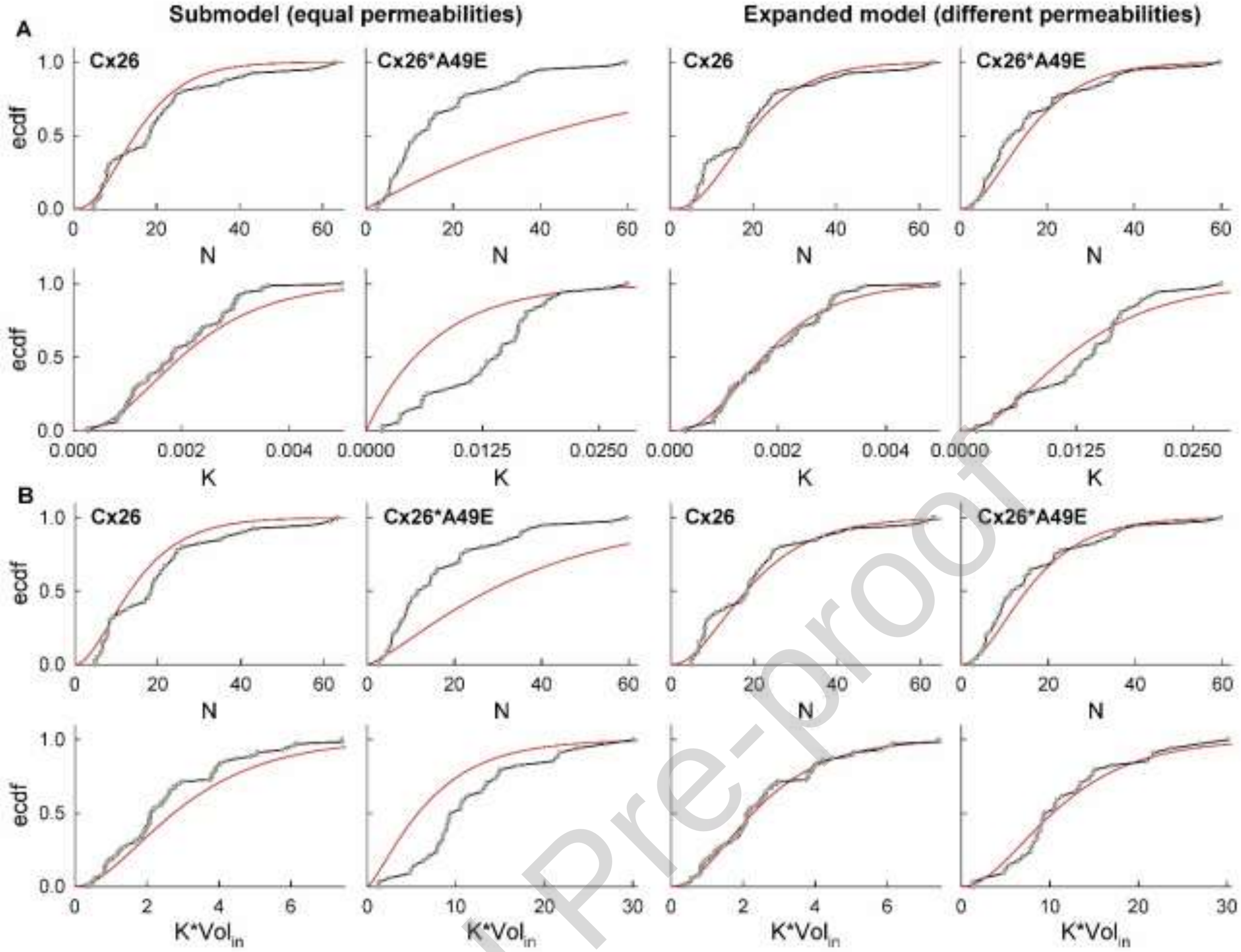

Fig. 4. Fits of gamma distribution using the proposed statistical model. (A) Fits to Cx26 and Cx26*A49E datasets using the restricted model (left panels) and expanded model (right panels). Grey circles and black lines represent empirical cumulative distribution functions (ecdfs); red lines indicate fitted gamma cumulative distribution functions. (**B**) Corresponding fits for datasets using permeability rate *K* values adjusted by estimated cell volumes Vol_{in}. Units of *K* are in a.u.· L/(µM·s), and Vol_{in} was measured in µm^3.

7. Statistical power of the proposed statistical model to detect differences in permeability

To evaluate the sensitivity of the proposed methodology in detecting differences in permeability ratio, we performed a simulation-based power analysis of the statistical test. In these simulations, we generated sets of random variables X and Y, representing the numbers of functional channels of different types, such as WT and mutant channels (N_{wt} and N_{mut}). The associated permeability datasets, PX and PY, were generated using the relationship $PX = P_X \cdot X$ and $PY = P_Y \cdot Y$, where P_X and P_Y are positive constants representing permeability coefficients of different channels.

For simplicity, we modelled X and Y using a gamma distribution with identical shapes and scale parameters ($\alpha_X = \alpha_Y$ and $\sigma_X = \sigma_Y$), selected to reflect values observed in the experimental data. The permeability coefficient P_X was fixed to 1, while P_Y was varied to obtain different ratios P_Y/P_X. According to the properties of the gamma random variables, permeability datasets PX and PY were described by a shape parameter $\alpha_{PX} = \alpha_{PY} = \alpha_X = \alpha_Y$ and scale parameters $\sigma_{PX} = P_X \cdot PX$ and $\sigma_{PY} = P_Y \cdot PY$. This allowed us to assess the probability of detecting a statistically significant difference between P_X and P_Y using the likelihood ratio test. For each sample size, we generated 1000 independent datasets of X, Y, PX, and PY and applied the likelihood ratio test. The fraction of cases where the test yielded p-values below 0.05 was taken as the statistical power (probability 1-β, where β denotes type II statistical). An example of the MATLAB code is provided in Supplementary data.

Simulation results in Fig. 5A show the dependence of test power on sample sizes n_X and n_Y (left panel) and n_{PX} and n_{PY} (right panel). In Fig. 5, the gamma distribution shape parameters were set to $\alpha_X = \alpha_Y = 2.40$, and the scale parameters to $\sigma_X = \sigma_Y = 8.00$. The power of the test increased similarly with increases in either n_X and n_Y, or n_{PX} and n_{PY}. Since n_{PX} and n_{PY} correspond to the number of fluorescence recordings in our methodology – data that is easier to collect in large amounts compared to electrophysiological conductance measurements – increasing n_{PX} and n_{PY} appears to be a more practical strategy for improving test power.

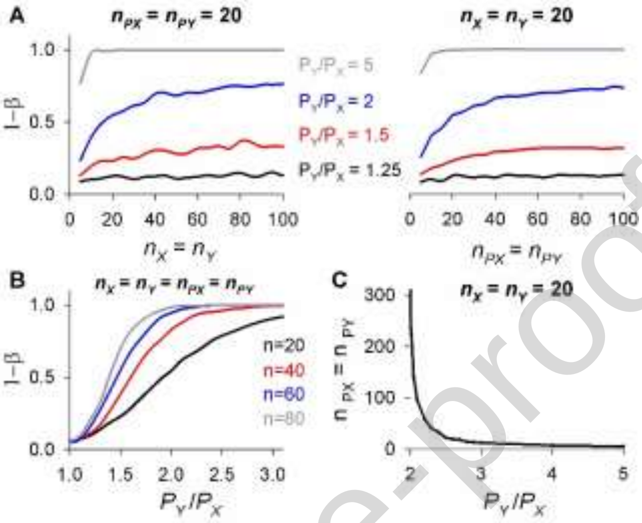

Fig. 5. Evaluation of the statistical power of the proposed method for comparing Cx hemichannel permeability. (A) Test power as a function of sample sizes of hemichannel conductance estimates (n_X and n_Y) and fluorescence intensity traces (n_{PX} and n_{PY}) at varying permeability ratios P_Y/P_X. (**B**) Test power curves as a function of the permeability ratio P_Y/P_X, evaluated for different sample sizes. (**C**) Required sample sizes of fluorescence intensity traces to achieve a statistical power of 0.80 across different P_Y/P_X ratios.

Fig. 5B illustrates the relationship between test power and the permeability ratio P_Y/P_X at fixed sample sizes. These data suggest that while the proposed test cannot reliably detect small permeability differences, it achieves acceptable power (~0.80 probability) for moderate sample sizes when the ratio $P_Y/P_X > 2$. Fig. 5C further confirms this by showing the minimum required sample size of P_X and P_Y (with $n_X = n_Y = 20$) needed to achieve a test power of 0.80. The required sample size decreases sharply once P_Y/P_X exceeds 2. For larger permeability differences, such as those observed in our study (where estimated $P_Y/P_X > 5$), the required sample size is relatively small (around 5-7 samples).

Our simulation data also demonstrated that these findings hold across different underlying distributions of *X* and *Y* (for example, varying shape α or scale β resulted in similar trends). Thus, this power analysis confirms that the proposed statistical test is robust in detecting permeability differences in electrophysiological and fluorescence imaging data. In our case, the observed permeability difference between WT Cx26 and Cx26*A49E hemichannels is large enough to be reliably detected by the proposed statistical approach.

Discussion

We present a methodology that enables the comparison of molecular permeabilities among different types of Cx hemichannels. The key feature of the approach is the integration of independently collected electrophysiological and fluorescence imaging data. Electrophysiological recordings provide measures of total conductance (g) and unitary conductance (γ). The value of g/γ provides a measure of the number of open channels, N. The changes in fluorescence intensity over time provide estimates of the product $P \cdot N$, where P represents the permeability of a single channel. By integrating data from different hemichannel types into a unified statistical model based on a likelihood ratio test, our methodology allows for rigorous comparisons of permeability differences.

Separating electrophysiological and fluorescent imaging data

The proposed methodology is technically less demanding than previously published techniques that attempt to measure the number of open channels and fluorescence changes within the same cells [20, 42-44]. Performing electrophysiological and fluorescent imaging experiments separately increases experimental flexibility, allowing these measurements to be conducted at different times. In practice, the approach should also enable the pooling of data from different laboratories or previously published studies.

To ensure the validity of pooled data, it is essential that the distribution of functional channel numbers in fluorescence imaging experiments be consistent with that in electrophysiological recordings. This requires using the same cell lines for a given hemichannel type. Additionally, experimental conditions influencing open-state probability – such as membrane voltage and extracellular divalent ion concentration – must be standardized. For Cx hemichannels, extracellular Ca^{2+} and Mg^{2+} concentrations are particularly important as they act to robustly modulate hemichannel currents [26, 57].

Importantly, our statistical model does not require identical channel number distributions between different Cx hemichannel types. This flexibility allows for cross-comparisons between datasets obtained from different cell types. However, for each hemichannel type, fluorescence imaging and electrophysiological data must be derived from the same cell line. Additional considerations include differences in resting membrane potential and potential differences in cell volumes.

Required sample sizes

A limitation of our methodology is that quite large datasets are needed to detect relatively small permeability differences. Simulations suggest that resolving permeability differences smaller than twofold requires datasets exceeding 500-1000 samples to achieve a statistical power of 0.80. In contrast, direct measurements of single-channel permeability via simultaneous electrophysiological and diffusion rate recordings [21, 43] likely require far fewer samples for comparable statistical significance.

However, this drawback can be partially offset particularly when permeability differences exceed twofold. Simulation data indicate that the statistical power of our test depends equally on the sizes of both electrophysiological and imaging datasets. Large fluorescence imaging datasets can be obtained efficiently using high-throughput tracer uptake/release assays, which are technically simpler than electrophysiological recordings and allow the collection of 5-20 samples per experiment. Automated cell detection and segmentation software can further streamline data analysis. When permeability differences exceed threefold, our approach may enable faster collection of sufficient amounts of data compared to more complex simultaneous measurement techniques.

Simplified diffusion model

Our methodology employs a simplified diffusion model based on Fick’s law and the GHK current equation to describe Cx hemichannel permeability. A similar approach was used in previous studies on Cx hemichannel permeability [40]. However, this model does not account for certain mechanistic features that are relevant for tracer uptake/release assays, such as subcellular spatial inhomogeneities or tracer binding.

The assumption of spatial homogeneity is justified when the characteristic diffusion time within a cell is much shorter than the experimental time window over which tracer uptake is quantified. This can be evaluated using basic diffusion theory. For three-dimensional Brownian motion, the mean-squared displacement is

$$\langle r^2 \rangle = 6 \cdot d \cdot t, \tag{25}$$

where *d* is the diffusion coefficient and *t* is the characteristic diffusion time. The latter is easily obtained by solving Eq. (25) for *t*. HeLa cells typically exhibit a relatively simple, non-branching morphology (see Fig. 2), with effective cytoplasmic radii in the 10-20 µm range and an average cytoplasmic distance to the nucleus of ~5-10 µm. Experimentally measured diffusion coefficient for DAPI in living cells is on the order of ~15 µm^2/s [58]. Using these values, the characteristic time for a molecule to diffuse across ~5-10 µm of cytoplasm is below one second, which is orders of magnitude shorter than the time scale over which tracer uptake is quantified. Therefore, intracellular concentration gradients are expected to equilibrate rapidly, making spatial homogeneity approximation reasonable.

Our model also assumes that fluorescence intensity is directly proportional to intracellular tracer concentration, despite the fact that some tracers, such as DAPI, only fluoresce upon DNA binding. As a result, the model is not suitable for describing fluorescence recordings that exhibit saturation, as it cannot distinguish between saturation limited by diffusion and that limited by binding. In such cases, a more advanced tracer uptake model incorporating intracellular binding kinetics and more complex cellular morphology could be applied instead, as was proposed in [59].

To minimize the impact of binding-related discrepancies, we restricted our analysis to the short initial segments of the fluorescence time courses, which can be adequately described by the linear model presented in Eqs. (18) and (20). A simple analysis provided here indicates that under these conditions, the proposed methodology remains valid.

To account for tracer binding to DNA or other intracellular substrates, denoted as *S*, we consider the concentration of the tracer-substrate complex, [C_{in}-*S*]. During the initial stage of the experiment, the total binding site concentration is much greater than the amount of bound tracer, and binding does not significantly deplete the intracellular free tracer concentration $C_{in}(t)$. Thus, the kinetics of [C_{in}-*S*] complex concentration can be approximated by the following ODE:

$$\frac{d[C_{in} - S](t)}{dt} = k_{on} \cdot C_{in} \cdot S - k_{off} \cdot [C_{in} - S](t). \tag{26}$$

Here, k_{on} and k_{off} are the association and dissociation rate constants, respectively, and *S* is the concentration of available binding sites. Assuming that the initial concentration of the complex is zero, the solution of Eq. (26) is:

$$[C_{in} - S](t) = \frac{k_{on} \cdot C_{in} \cdot S}{k_{off}} \cdot \left(1 - \exp(-k_{off} \cdot t)\right). \tag{27}$$

At early time points, when the product $k_{off} \cdot t$ is sufficiently small, the exponential term in the Eq. (27) can be approximated using a first-order Taylor series expansion, yielding the following linear function:

$$[C_{in} - S](t) = k_{on} \cdot C_{in} \cdot S \cdot t. \tag{28}$$

This result supports the use of our simplified linear model to describe the initial uptake phase, even when tracer binding occurs. Nevertheless, the inclusion of binding kinetics introduces additional parameters, such as k_{on} and *S*, which may contribute to variability in the estimated permeability rates. This should be taken into account when comparing hemichannel permeability across different experimental conditions or different cell lines.

Applicability to other types of channels

Our methodology, applied here to compare permeability of WT Cx26 and Cx26*A49E hemichannels, can be extended to functional gap junction channels. In our previous study [19], we implemented a low-throughput version of this approach, in which electrophysiological recordings and fluorescence imaging were performed sequentially in the same paired cells to estimate gap junction channel permeability. The framework can, in principle, be adapted to high-throughput fluorescence imaging as proposed in this study. This would require incorporating mathematical models of intercellular diffusion, as described in [19], and modifying the cell-segmentation pipeline to identify gap junctional plaques between cell pairs.

The proposed methodology is also logically applicable to other large-pore channels permeable to small tracer molecules. Such channels include pannexins (Panx), calcium homeostasis modulators (CALHMs), and volume-regulated anion channels (VRACs).

Similar to Cxs, Panxs form hemichannels permeable to small molecules, such as ATP [60]. Only three Panx isoforms have been identified in humans [61], but at least one is expressed in most mammalian tissues. Changes in Panx expression are associated with various pathological conditions in nervous system [62, 63] and skeletal disorders [64, 65], and mutations in Panx1 gene were recently linked to genetic diseases, such as human oocyte death [66].

CALHM channels share functional properties with Cx hemichannels, such as voltage and Ca^{2+} sensitivity and permeability to small molecules [67, 68]. CALHM channels are important in neuronal excitability and muscle cell function [69]. Mutations in CALHM1 are associated with Alzheimer's disease [70, 71], while CALHM3 channels play a role in taste perception [72, 73]. Interestingly, CALHM proteins can form oligomeric assemblies with varying protomer number [74, 75], each conceivably exhibiting differences in permeability.

VRAC channels, formed of leucine-rich repeat-containing (LRRC) proteins, regulate cell volume through Cl^- and osmolyte transport [76-78]. Mutations in the LRRC8A gene are linked to immune-deficiency disorder agammaglobulinemia [79, 80] while LRRC8C mutations affect cell volume regulation, contributing to various disorders [81]. VRAC permeability varies with subunit composition, influencing metabolite transport [82].

Thus, evaluating the permeability of other large-pore channels is essential for understanding their physiological and pathological roles.

Author Contribution

T.K. and M.S. conceived the study. T.K., L.Kr., V.K.V., and M.S. designed the research. T.K. and L.Kr. performed electrophysiological and fluorescent imaging experiments. L.Ke., A.K., and D.C. developed the deep learning-based cell segmentation system and performed its testing. M.S. developed the mathematical and statistical models. A.C. and M.S. conducted data analysis and simulations. T.K., V.K.V., and M.S. prepared the manuscript.

Funding sources

This work was supported by the project Centre of Excellence for Sustainable Living and Working (SustAInLivWork), co-funded by the European Union's Horizon Europe programme (Grant Agreement No. 101059903) and the European Union Funds' Investments 2021–2027 (Project No. 10-042-P-0001).

Declaration of competing interests

The authors declare that they have no known competing financial interests or personal relationships that could have appeared to influence the work reported in this paper.

References

[1] D.L. Paul, L. Ebihara, L.J. Takemoto, K.I. Swenson, D.A. Goodenough, J.Cell Biol., 115 (1991) 1077-1089.

[2] L. Ebihara, E. Steiner, J.Gen.Physiol., 102 (1993) 59-74.

[3] S.H. DeVries, E.A. Schwartz, J.Physiol., 445 (1992) 201-230.

[4] R.P. Malchow, H. Qian, H. Ripps, J.Neurosci.Res., 35 (1993) 237-245.

[5] R.P. Malchow, H. Qian, H. Ripps, J Gen Physiol, 104 (1994) 1039-1055.

[6] J.E. Contreras, J.C. Saez, F.F. Bukauskas, M.V. Bennett, Proc Natl Acad Sci U S A, 100 (2003) 11388-11393.

[7] M. Romanello, P. D'Andrea, Journal of Bone & Mineral Research, 16 (2001) 1465-1476.

[8] C.E. Stout, J.L. Costantin, C.C. Naus, A.C. Charles, J. Biol. Chem., 277 (2002) 10482-10488.

[9] L. Leybaert, K. Braet, W. Vandamme, L. Cabooter, P.E. Martin, W.H. Evans, Cell Commun Adhes, 10 (2003) 251-257.

[10] S.A. John, R. Kondo, S.Y. Wang, J.I. Goldhaber, J.N. Weiss, J Biol Chem, 274 (1999) 236-240.

[11] J.E. Contreras, H.A. Sanchez, E.A. Eugenin, D. Speidel, M. Theis, K. Willecke, F.F. Bukauskas, M.V. Bennett, J.C. Saez, Proc Natl Acad Sci U S A, 99 (2002) 495-500.

[12] J.A. Orellana, N. Froger, P. Ezan, J.X. Jiang, M.V. Bennett, C.C. Naus, C. Giaume, J.C. Saez, J Neurochem, 118 (2011) 826-840.

[13] M.V. Bennett, J.M. Garré, J.A. Orellana, F.F. Bukauskas, M. Nedergaard, J.C. Sáez, Brain Res., 1487 (2012) 3-15.

[14] G. Sohl, K. Willecke, Cardiovasc. Res., 62 (2004) 228-232.

[15] K. Willecke, J. Eiberger, J. Degen, D. Eckardt, A. Romualdi, M. Guldenagel, U. Deutsch, G. Sohl, Biol. Chem., 383 (2002) 725-737.

[16] J.L. Esseltine, D.W. Laird, Trends Cell Biol, 26 (2016) 944-955.

[17] A.L. Harris, Prog Biophys Mol Biol., 94 (2007) 120-143.

[18] D.B. Hansen, T.H. Braunstein, M.S. Nielsen, N. MacAulay, FEBS Lett, 588 (2014) 1446-1457.

[19] L. Kraujaliene, T. Kraujalis, M. Snipas, V.K. Verselis, J Gen Physiol, 156 (2024).

[20] J. Xu, B.J. Nicholson, Life (Basel), 13 (2023).

[21] P.S. Gaete, D. Kumar, C.I. Fernandez, J.M. Valdez Capuccino, A. Bhatt, W. Jiang, Y.C. Lin, Y. Liu, A.L. Harris, Y.L. Luo, J.E. Contreras, Proc Natl Acad Sci U S A, 121 (2024) e2403903121.

[22] B.S. Nielsen, J.S. Alstrom, B.J. Nicholson, M.S. Nielsen, N. MacAulay, J Biol Chem, 292 (2017) 19999-20009.

[23] M.A. Retamal, C.J. Cortes, L. Reuss, M.V. Bennett, J.C. Saez, Proc Natl Acad Sci U S A, 103 (2006) 4475-4480.

[24] J.M. Gomez-Hernandez, M. de Miguel, B. Larrosa, D. Gonzalez, L.C. Barrio, Proc Natl Acad Sci U S A, 100 (2003) 16030-16035.

[25] M.A. Retamal, N. Froger, N. Palacios-Prado, P. Ezan, P.J. Saez, J.C. Saez, C. Giaume, J Neurosci, 27 (2007) 13781-13792.

[26] L. Ebihara, X. Liu, J.D. Pal, Biophys J, 84 (2003) 277-286.

[27] H.A. Sanchez, G. Mese, M. Srinivas, T.W. White, V.K. Verselis, J Gen Physiol, 136 (2010) 47-62.

[28] H.A. Sanchez, K. Villone, M. Srinivas, V.K. Verselis, J Gen Physiol, 142 (2013) 3-22.

[29] H.A. Sanchez, N. Slavi, M. Srinivas, V.K. Verselis, J Gen Physiol, 148 (2016) 25-42.

[30] I.E. Garcia, F. Villanelo, G.F. Contreras, A. Pupo, B.I. Pinto, J.E. Contreras, T. Perez-Acle, O. Alvarez, R. Latorre, A.D. Martinez, C. Gonzalez, J Gen Physiol, 150 (2018) 697-711.

[31] M. Bicego, M. Beltramello, S. Melchionda, M. Carella, V. Piazza, L. Zelante, F.F. Bukauskas, E. Arslan, E. Cama, S. Pantano, R. Bruzzone, P. D'Andrea, F. Mammano, Hum Mol Genet, 15 (2006) 2569-2587.

[32] G. Mese, V. Valiunas, P.R. Brink, T.W. White, Am J Physiol Cell Physiol, 295 (2008) C966-974.

[33] P.V. Mhaske, N.A. Levit, L. Li, H.Z. Wang, J.R. Lee, Z. Shuja, P.R. Brink, T.W. White, Am J Physiol Cell Physiol, 304 (2013) C1150-1158.

[34] J.C. Wingard, H.B. Zhao, Front Cell Neurosci, 9 (2015) 202.

[35] M. Srinivas, V.K. Verselis, T.W. White, Biochim Biophys Acta Biomembr, 1860 (2018) 192-201.

[36] V.K. Verselis, M.P. Trelles, C. Rubinos, T.A. Bargiello, M. Srinivas, J Biol Chem, 284 (2009) 4484-4493.

[37] S. Maeda, S. Nakagawa, M. Suga, E. Yamashita, A. Oshima, Y. Fujiyoshi, T. Tsukihara, Nature, 458 (2009) 597-602.

[38] J.B. Myers, B.G. Haddad, S.E. O'Neill, D.S. Chorev, C.C. Yoshioka, C.V. Robinson, D.M. Zuckerman, S.L. Reichow, Nature, 564 (2018) 372-377.

[39] A.L. Harris, C.G. Bevans, Methods Mol Biol, 154 (2001) 357-377.

[40] R.G. Johnson, H.C. Le, K. Evenson, S.W. Loberg, T.M. Myslajek, A. Prabhu, A.M. Manley, C. O'Shea, H. Grunenwald, M. Haddican, P.M. Fitzgerald, T. Robinson, B.A. Cisterna, J.C. Saez, T.F. Liu, D.W. Laird, J.D. Sheridan, J Membr Biol, 249 (2016) 713-741.

[41] J.E. Linley, Methods Mol Biol, 998 (2013) 149-157.

[42] P.S. Gaete, M.A. Lillo, W. Lopez, Y. Liu, W. Jiang, Y. Luo, A.L. Harris, J.E. Contreras, J Gen Physiol, 152 (2020).

[43] P.S. Gaete, J.E. Contreras, Methods Enzymol, 654 (2021) 271-293.

[44] V. Valiunas, J Gen Physiol, 119 (2002) 147-164.

[45] H.A. Sanchez, L. Kraujaliene, V.K. Verselis, The Journal of general physiology, 156 (2024).

[46] F. Zonta, G. Polles, G. Zanotti, F. Mammano, J Biomol Struct Dyn, 29 (2012) 985-998.

[47] J. Kapuscinski, Biotechnic & Histochemistry, 70 (1995) 220-233.

[48] S. Hamann, J.F. Kiilgaard, T. Litman, F.J. Alvarez-Leefmans, B.R. Winther, T. Zeuthen, Journal of Fluorescence, 12 (2002) 139-145.

[49] M.F.K. Wills, C.B. Alejo, N. Hundt, A.J. Hudson, I.C. Eperon, Comput Struct Biotechnol J, 23 (2024) 918-928.

[50] J. Jang, C. Wang, X. Zhang, H.J. Choi, X. Pan, B. Lin, Y. Yu, C. Whittle, M. Ryan, Y. Chen, K. Lee, Cell Rep Methods, 1 (2021).

[51] C.F. Otesteanu, R. Caldelari, V. Heussler, R. Sznitman, Comput Struct Biotechnol J, 24 (2024) 334-342.

[52] Y. Hyun, D. Kim, Comput Struct Biotechnol J, 21 (2023) 879-888.

[53] G. Kanaporis, P.R. Brink, V. Valiunas, Am J Physiol Cell Physiol., 300 (2011) C600-609.

[54] P. Fan, Y. Zhang, X. Guo, C. Cai, M. Wang, D. Yang, Y. Li, J. Tu, L.A. Crum, J. Wu, D. Zhang, Theranostics, 7 (2017) 4894-4908.

[55] L. Kraujaliene, T. Kraujalis, M. Snipas, V.K. Verselis, Journal of General Physiology, 156 (2024).

[56] H.A. Sánchez, G. Mese, M. Srinivas, T.W. White, V.K. Verselis, J Gen Physiol., 136 (2010) 47-62.

[57] V.K. Verselis, M. Srinivas, J Gen Physiol, 132 (2008) 315-327.

[58] D.K. Sasmal, S. Ghosh, A.K. Das, K. Bhattacharyya, Langmuir, 29 (2013) 2289-2298.

[59] J.M. Nitsche, H. Chang, P.A. Weber, B.J. Nicholson, Biophys J., 86 (2004) 2058-2077.

[60] L. Bao, S. Locovei, G. Dahl, FEBS Lett., 572 (2004) 65-68.

[61] R. Bruzzone, S.G. Hormuzdi, M.T. Barbe, A. Herb, H. Monyer, Proc Natl Acad Sci U S A, 11 (2003) 13644-13649.

[62] S. Penuela, L. Harland, J. Simek, D.W. Laird, Biochem J, 461 (2014) 371-381.

[63] A.K. Yeung, C.S. Patil, M.F. Jackson, J Neurochem, 154 (2020) 468-485.

[64] L.A. Cea, M.A. Riquelme, A.A. Vargas, C. Urrutia, J.C. Saez, Front Physiol, 5 (2014) 139.

[65] Y. Luo, S. Zheng, W. Xiao, H. Zhang, Y. Li, Bone Res, 12 (2024) 26.

[66] Q. Sang, Z. Zhang, J. Shi, X. Sun, B. Li, Z. Yan, S. Xue, A. Ai, Q. Lyu, W. Li, J. Zhang, L. Wu, X. Mao, B. Chen, J. Mu, Q. Li, J. Du, Q. Sun, L. Jin, L. He, S. Zhu, Y. Kuang, L. Wang, Sci Transl Med, 11 (2019).

[67] A.P. Siebert, Z. Ma, J.D. Grevet, A. Demuro, I. Parker, J.K. Foskett, J Biol Chem, 288 (2013) 6140-6153.

[68] Z.M. Ma, A.P. Siebert, K.H. Cheung, R.J. Lee, B. Johnson, A.S. Cohen, V. Vingtdeux, P. Marambaud, J.K. Foskett, P Natl Acad Sci USA, 109 (2012) E1963-E1971.

[69] R. Polfer, H. Furukawa, J Physiol-London, (2024).

[70] U. Dreses-Werringloer, J.C. Lambert, V. Vingtdeux, H.T. Zhao, H. Vais, A. Siebert, A. Jain, J. Koppel, A. Rovelet-Lecrux, D. Hannequin, F. Pasquier, D. Galimberti, E. Scarpini, D. Mann, C. Lendon, D. Campion, P. Amouyel, P. Davies, J.K. Foskett, F. Campagne, P. Marambaud, Cell, 133 (2008) 1149-1161.

[71] F. Rubio-Moscardo, N. Setó-Salvia, M. Pera, M. Bosch-Morato, C. Plata, O. Belbin, G. Gené, O. Dols-Icardo, M. Ingelsson, S. Helisalmi, H. Soininen, M. Hiltunen, V. Giedraitis, L. Lannfelt, A. Frank, M.J. Bullido, O. Combarros, P. Sánchez-Juan, M. Boada, L. Tárraga, P. Pastor, J. Pérez-Tur, M. Baquero, J.L. Molinuevo, R. Sánchez-Valle, P. Fuentes-Prior, J. Fortea, R. Blesa, F.J. Muñoz, A. Lleó, M.A. Valverde, J. Clarimón, Plos One, 8 (2013).

[72] Z.M. Ma, A. Taruno, M. Ohmoto, M. Jyotaki, J.C. Lim, H. Miyazaki, N. Niisato, Y. Marunaka, R.J. Lee, H. Hoff, R. Payne, A. Demuro, I. Parker, C.H. Mitchell, J. Henao-Mejia, J.E. Tanis, I. Matsumoto, M.G. Tordoff, J.K. Foskett, Neuron, 98 (2018) 547-+.

[73] Z.M. Ma, A. Taruno, M. Tordoff, I. Matsumoto, M. Ohmoto, J.E. Tanis, J.K. Foskett, Chem Senses, 43 (2018) E135-E136.

[74] K. Demura, T. Kusakizako, W. Shihoya, M. Hiraizumi, K. Nomura, H. Shimada, K. Yamashita, T. Nishizawa, A. Taruno, O. Nureki, Sci Adv, 6 (2020).

[75] J.L. Syrjanen, K. Michalski, T.H. Chou, T. Grant, S.L. Rao, N. Simorowski, S.J. Tucker, N. Grigorieff, H. Furukawa, Nature Structural & Molecular Biology, 27 (2020) 150-+.

[76] M.D. Cahalan, R.S. Lewis, Soc Gen Physiol Ser, 43 (1988) 281-301.

[77] F.K. Voss, F. Ullrich, J. Munch, K. Lazarow, D. Lutter, N. Mah, M.A. Andrade-Navarro, J.P. von Kries, T. Stauber, T.J. Jentsch, Science, 344 (2014) 634-638.

[78] Z. Qiu, A.E. Dubin, J. Mathur, B. Tu, K. Reddy, L.J. Miraglia, J. Reinhardt, A.P. Orth, A. Patapoutian, Cell, 157 (2014) 447-458.

[79] A. Sawada, Y. Takihara, J.Y. Kim, Y. Matsuda-Hashii, S. Tokimasa, H. Fujisaki, K. Kubota, H. Endo, T. Onodera, H. Ohta, K. Ozono, J. Hara, J Clin Invest, 112 (2003) 1707-1713.

[80] B. Konig, T. Stauber, Biophys J, 116 (2019) 1185-1193.

[81] M. Quinodoz, S. Rutz, V. Peter, L. Garavelli, A.M. Innes, E.F. Lehmann, S. Kellenberger, Z. Peng, A. Barone, B. Campos-Xavier, S. Unger, C. Rivolta, R. Dutzler, A. Superti-Furga, EMBO J, 44 (2025) 413-436.

[82] T. Stauber, Biol Chem, 396 (2015) 975-990.

Author Contribution

T.K. and M.S. conceived the study. T.K., L.Kr., V.K.V., and M.S. designed the research. T.K. and L.Kr. performed electrophysiological and fluorescent imaging experiments. L.Ke., A.K., and D.C. developed the deep learning-based cell segmentation system and performed its testing. M.S. developed the mathematical and statistical models. A.C. and M.S. conducted data analysis and simulations. T.K., V.K.V., and M.S. prepared the manuscript.

Declaration of Competing interests

The authors declare that they have no known competing financial interests or personal relationships that could have appeared to influence the work reported in this paper.

Highlights

- Statistical model integrates fluorescence imaging and electrophysiology
- Imaging and electrophysiology data can be obtained from separate cells
- Allows leveraging high-throughput fluorescent tracer uptake/release assays
- AI-based cell detection system streamline extraction of imaging data
- Applicable for permeability comparison of large-pore channels